Morphology development of helical structure in bicomponent fibers during spinning process

Xiaomin Zhang [1], Jiawei Chen [1], Yongchun Zeng [*]

College of Textiles, Donghua University, Shanghai, 201620, China

ARTICLE INFO

ABSTRACT

The present study is the first to describe the modeling of the morphology development of helical structures in melt-blown and electrospun fibers by calculating the intrinsic curvature within the bicomponent fibers. The theoretical model incorporates a physical model for the intrinsic curvature of the bicomponent jet with jet dynamics in the applied physical fields. We study the mechanical behaviors responsible for intrinsic curvature due to the non-uniform stretch of the bicomponent jet. Based on this model, we report on the development of intrinsic curvature of melt-blown PP/TPU and electrospun CA/TPU fibers. Several parameter effects on the intrinsic curvature are predicted by virtue of this model, which suggests the fabrication control of helical micro/nanofibers.

1. Introduction

Both melt blowing and electrospinning are the most common technologies used for producing micro/nanofibers. In the melt blowing process, polymer melt is extruded from the spinneret and drawn down by high-speed hot air to produce fibers. During electrospinning, polymer solution flows down from the spinneret and is accelerated to the collector via electric field provided by a high-voltage power supply. To gain fundamental insight into the melt blowing and electrospinning processes, dynamical models have been developed by several research groups [1–6]. Bioinspired helical structures with dimensions of different orders of magnitude have found to be high specific surface area and good mechanical performance. Helical fibers at micro/nanoscale have been reported to be fabricated with two different polymers through bicomponent melt blowing or electrospinning processes [7–12]. However, the mechanical behavior of the bicomponent jet remains elusive.

It is difficult to experimentally resolve the individual roles of the material properties and processing parameters in morphology of the helical fibers in the spinning processes. This is the source of our motivation to model the morphology development during the spinning process. In our previous studies [11–14], helical micro/nanofibers have been fabricated through melt blowing and electrospinning, and the formation mechanism has been discussed. Since the two components have distinct intrinsic properties, they would be stretched to different degrees in the applied external physical fields when they were spun individually, resulting in unequal strains, which is believed to be the root cause of bending into helix when they were spun contemporary through bicomponent spinning method. The curvature generation in plant tendrils and bimetal thermostats [15,16] shows a striking resemblance to the helical structure formation during spinning, based on which we present a theoretical model to calculate the intrinsic curvature of the bicomponent fiber.

Our group has previously presented dynamical models to simulate jet motion in the processes of melt blowing and electrospinning [17,18]. In this manuscript, physical expressions for the intrinsic curvature of the bicomponent jet derived from the expressions for a heated bimetallic strip, in conjunction with jet dynamics in the applied physical fields (i.e. airflow field and electric field) is developed to explore the helical morphology development in bicomponent fibers during melt blowing and electrospinning. Polymer components of Polypropylene (PP)/Thermoplastic Polyurethane (TPU) in the melt blowing process and Cellulose Acetate (CA)/TPU in electrospinning are employed in the model and the experiments. The longitudinal strain difference and resultant intrinsic curvature within the bicomponent jet is calculated. Based on the theoretical results, the prediction of the parameter effects is carried out.

---

* Corresponding author.
  E-mail address: yongchun@dhu.edu.cn (Y. Zeng).
[1] X.Z. and J.C. contributed equally to this work.

2. Theoretical model

2.1. Physical model construction of Bi-layer strip

In this study, a parallel arranged bicomponent polymer jet is created from the spinnerets of melt blowing and electrospinning. The bicomponent jet, containing component A and component B, is illustrated in Fig. 1a. In the modeling, the polymer jet is divided into a series of bi-jet elements. As depicted in the insertion of Fig. 1a, in the ith element, two parts consisting of different components are closely adjacent to each other with a rectangular interface of w_i in width. Based on the fixed interface, these two semi-cylinders are transformed into two rectangular cross-section strips by keeping the volume constant. The two strips, which are named as layer A_i and layer B_i, form a bi-layer strip $(AB)_i$. The involved two layers possess elastic modulus of G_A, G_B, viscosity of μ_A, μ_B, width of, w_{A_i}, w_{B_i} (here, $w_{A_i} = w_{B_i} = w_i$), and thickness of $h_{A_i} = \frac{s\pi d_i^2}{4w_{A_i}}$, $h_{B_i} = \frac{(1-s)\pi d_i^2}{4w_{B_i}}$, respectively, where d_i is the diameter of the ith element, and s is the volume proportion of Component A in the bi-jet. As depicted in Fig. 1b, the width of the two layers is determined by the diameter of the bicomponent jet and their proportion in the jet, where we get:

$$w_i = d_i \sin \frac{\theta}{2} \tag{1}$$

where θ is the radian of the archy cross-section of component A and is determined by s:

$$\frac{d_i^2(\theta - \sin\theta)}{8} = \frac{s\pi d_i^2}{4} \tag{2}$$

Owing to the distinct intrinsic properties, the bending behavior of the bi-layer strip is analogous to the generation of curvature of a heated bimetallic strip that bends due to the differential expansion of its constituent elements [16]. In the same applied physical field (i.e., melt blowing airflow field and electrospinning electric field), the two components is subjected to different longitudinal stress. Thus the two layers should have been stretched to unequal longitudinal strain values of $\varepsilon_{A_i}^*$ and $\varepsilon_{B_i}^*$. In the bi-layer strip $(AB)_i$, layer A_i and B_i are permanently bonded together and no relative displacement would take place at the interface. To gain equilibrium configuration, the two layers are stretched to longitudinal strains of ε_{A_i} and ε_{B_i} with an intrinsic curvature of k_i.

The polymer jet can be considered as a viscoelastic Maxwellian liquid jet which consists of an ideal elastic spring attached to an ideal dashpot [4]. Accordingly, the bi-layer strip $(AB)_i$ in our model is considered as two bead-viscoelastic element chain, in which layer A_i consists of Bead a_i and its two neighboring beads, so does B_i (depicted in Fig. 2).

In the same applied physical field, if the two layers are not bonded to each other, which as if they were spun individually, the two layers should have been stretched to unequal strain values of $\varepsilon_{A_i}^*$ and $\varepsilon_{B_i}^*$:
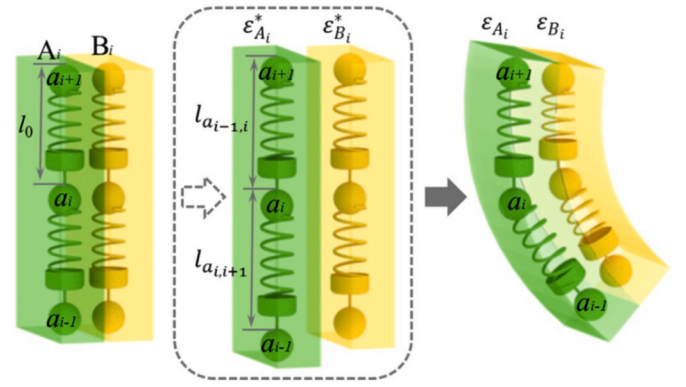

Fig. 2. Schematic of the transformation of bi-layer strip $(AB)_i$ into a bent one.

$$\varepsilon_{A_i}^* = \frac{l_{a_{i-1,\,i}} + l_{a_{i,\,i+1}} - 2l_0}{2l_0 S_{A_i}} \tag{3}$$

where $S_{A_i} = \frac{s\pi d_i^2}{4}$ is the cross sectional area of Layer A_i at Bead a_i. $l_{a_{i-1,\,i}}$ and $l_{a_{i,\,i+1}}$ are the length of jet segment (a_{i-1}, a_i) and (a_i, a_{i+1}), respectively, and l_0 is their initial length. The stress $\sigma_{a_{i-1,\,i}}$ that pulls Bead a_{i-1} back to Bead a_i is then given by:

$$\frac{d\sigma_{a_{i-1,\,i}}}{dt} = G_A \frac{dl_{a_{i-1,\,i}}}{l_{a_{i-1,\,i}}\,dt} - \frac{G_A}{\mu_A}\sigma_{a_{i-1,\,i}} \tag{4}$$

where t is time.

At the equilibrium state, both force and torque are balanced in the bicomponent jet, described as following equations:

$$F_{A_i} + F_{B_i} = 0 \tag{5}$$

$$F_{A_i}h_{A_i} \Big/ 2 + F_{B_i}h_{B_i} \Big/ 2 = k_i\left[G_A \frac{w_{A_i}h_{A_i}^3}{12} + G_B \frac{w_{B_i}h_{B_i}^3}{12}\right] \tag{6}$$

$$F_{A_i} = \varepsilon_{A_i}G_A h_{A_i} w_{A_i} \tag{7a}$$

$$F_{B_i} = \varepsilon_{B_i}G_B h_{B_i} w_{B_i} \tag{7b}$$

The condition of forming the bi-layer strip is that the strains on the interface of the two components are identically equal and is given by:

$$\varepsilon_{A_i}^* + \frac{F_{A_i}}{G_A h_{A_i} w_{A_i}} + \frac{k_i h_{A_i}}{2} = \frac{k_i h_{B_i}}{2} + \frac{F_{B_i}}{G_B h_{B_i} w_{B_i}} + \varepsilon_{B_i}^* \tag{8}$$

Solving the above system of equations, we obtain an expression for the intrinsic curvature k_i of strip $(AB)_i$:
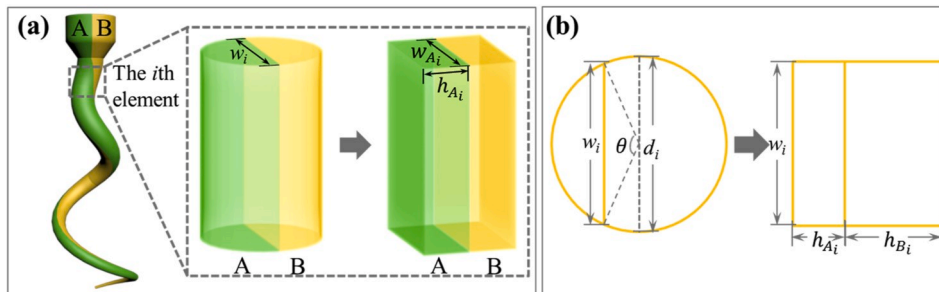

Fig. 1. (a) Illustration of bicomponent jet model, inserted with the bi-layer strip $(AB)_i$ (b) schematic of the transformation of a round cross-section of the ith element into a rectangular one.

$$k_i = \frac{6\left(\varepsilon_{A_i}^* - \varepsilon_{B_i}^*\right)(1+p)^2}{(h_{A_i} + h_{B_i})\left[3(1+p)^2 + (1+pq)\left(p^2 + \frac{1}{pq}\right)\right]} \tag{9}$$

where $p = \frac{h_{A_i}}{h_{B_i}} = \frac{s}{1-s}$ represents the volume ratio of two polymers, and $q = G_A/G_B$ is the ratio of elastic modulus of the two polymers, representing discrepancy between their elasticity properties.

The expression above indicates that the intrinsic curvature k_i is determined by the strain difference $\Delta\varepsilon_i^*$ ($\Delta\varepsilon_i^* = \varepsilon_{A_i}^* - \varepsilon_{B_i}^*$), the volume ratio p and the ratio of elastic modulus q of the two components, and jet diameter d_i.

2.2. Dynamics of A jet in the applied physical fields

To work out the intrinsic curvature k_i, it is necessary to figure out $\varepsilon_{A_i}^*$, $\varepsilon_{B_i}^*$, and d_i. $\varepsilon_{A_i}^*$ and $\varepsilon_{B_i}^*$ are, respectively, the strains occur when Component A and Component B are spun individually. At the same time, the jet diameter d_i is contributed by and the diameters of the two components d_{A_i} and d_{B_i} under the circumstance that they are spun individually and is given by:

$$d_i = sd_{A_i} + (1-s)d_{B_i} \tag{10}$$

The bead-viscoelastic element jet model shown in Fig. 3 is to describe the motion of the jet in the spinning processes. The model for simulating jet motion in the melt blowing and electrospinning processes [17,18], which has been previously developed by our group, is applied to calculate $\varepsilon_{A_i}^*$, $\varepsilon_{B_i}^*$, h_{A_i} and h_{B_i} numerically.

Jet temperature should be considered in the melt blowing process, and is known to be determined by the distance from the jet to the spinneret [3]. Here in, we assume that the temperatures of the two components are identical at the same Z-coordinate and the heat transfer between the polymers of different components is not considered.

In the external physical field, Bead i is subjected to various external forces $\mathbf{F}_{ex}$, internal forces $\mathbf{F}_{in}$, and bending restoring force $\mathbf{F}_b$. According to Newton's second law, we obtain the equation as follow:

$$m_i \frac{d^2\mathbf{R}_i}{d^2t} = \mathbf{F}_{ex_i} + \mathbf{F}_{in_i} + \mathbf{F}_{b_i} \tag{11}$$

where $\mathbf{R}_i = \mathbf{i}x_i + \mathbf{j}y_i + \mathbf{k}z_i$ is the coordinate of Bead i, and $\mathbf{i}$, $\mathbf{j}$, and $\mathbf{k}$ are unit vectors in the cartesian coordinate system. In our model, the mass of bead i is contributed by its adjacent jet segments (i-1, i) and (i, i+1), thus, m_i is described as

$$m_i = \frac{1}{2}\rho_f\left(\frac{\pi d_{i-1,\,i}^2}{4}l_{i-1,\,i} + \frac{\pi d_{i,\,i+1}^2}{4}l_{i,\,i+1}\right) \tag{12}$$
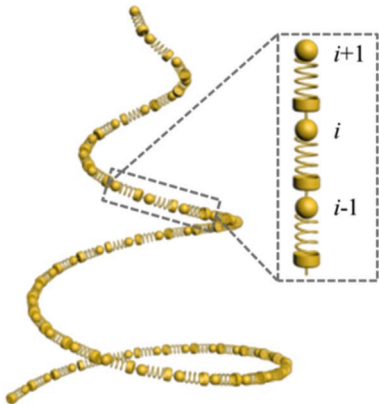

Fig. 3. Schematic of the bead-viscoelastic element jet model.

where $d_{i,\,i+1}$ and $d_{i-1,\,i}$ are the diameters of jet segment (i-1, i) and (i, i+1), respectively, and ρ_f is the density of polymer melt in melt blowing, or polymer solution in electrospinning. The length of segment (i-1, i) is as follows:

$$l_{i-1,\,i} = \left[(x_i - x_{i-1})^2 + (y_i - y_{i-1})^2 + (z_i - z_{i-1})^2\right]^{1/2} \tag{13}$$

2.2.1. External force

In the melt blowing process, the external forces include aerodynamic force exerted by the airflow field and gravity. During electrospinning, the external forces include electric force imposed by the electric field, gravity, and air drag force.

The aerodynamic force $\mathbf{F}_{di}$ on Bead i is contributed by jet segments (i-1, i) and (i, i+1), written as $\mathbf{F}_{di-1,i}^i$ and $\mathbf{F}_{di,i+1}^i$. In addition, for the segment (i-1, i), the aerodynamic force should be broken down into the friction drag force $\mathbf{F}_{fi-1,\,i}^i$ parallel to the jet axis, and the pressure drag force $\mathbf{F}_{Pi-1,\,i}^i$ normal to the jet axis. Then we get

$$\mathbf{F}_{di} = \frac{1}{2}\left(\mathbf{F}_{di-1,i}^i + \mathbf{F}_{di,i+1}^i\right) \tag{14}$$

$$\mathbf{F}_{di-1,i}^i = \mathbf{F}_{fi-1,i}^i + \mathbf{F}_{Pi-1,i}^i \tag{15}$$

$$\mathbf{F}_{fi-1,i}^i = \frac{1}{2}C_f\rho_a(\mathbf{v}_{ri}\cdot\mathbf{f}_t)^2\pi d_{i-1,i}l_{i-1,i}\cdot\mathbf{f}_t \tag{16}$$

$$\mathbf{F}_{Pi-1,i}^i = \frac{1}{2}C_P\rho_a(\mathbf{v}_{ri}\cdot\mathbf{f}_n)^2\pi d_{i-1,i}l_{i-1,i}\cdot\mathbf{f}_n \tag{17}$$

where ρ_a is the air density, C_f and C_p are respectively the friction drag coefficient and pressure coefficient. $\mathbf{f}_t$ is the unit vector parallel to the jet axis, and $\mathbf{f}_n$ is correspondingly the unit vector normal to the jet axis. $\mathbf{v}_{ri}$ is the relative speed between the air and Bead i:

$$\mathbf{v}_{ri} = \mathbf{v}_{ai} - \mathbf{v}_{fi} \tag{18}$$

where $\mathbf{v}_{ai}$ and $\mathbf{v}_{fi}$ are the air and jet velocities at Bead i.

Gravity is given by:

$$\mathbf{F}_{gi} = m_i g\mathbf{k} \tag{19}$$

where g is the acceleration of gravity.

The electric force on Bead i imposed by the electric field is as follows:

$$\mathbf{F}_{ei} = e\mathbf{E}_i \tag{20}$$

where $\mathbf{E}_i = E_{xi}\mathbf{i} + E_{yi}\mathbf{j} + E_{zi}\mathbf{k}$ is the electric field intensity at Bead i, e is the charge possessed by each bead which is assumed not change with the time. Based on the fact that the charge on the jet is composed of surface charge and inner current of the jets [19], we obtain the charge e as

$$e = \pi d_0^2 KE_0 + \pi d_0 l_0 \tau_0 \tag{21}$$

where K is the conductivity of the liquid, d_0, l_0, E_0, and τ_0 are the initial diameter, jet segment length, electric field intensity, and surface charge density at initial state.

The gravity and air drag force on the electrospun jet are neglected because they are small in comparison with the electric force [4].

2.2.2. Internal force

In the melt blowing process, viscoelastic force generated between beads is the only internal force. In electrospinning, in addition to the viscoelastic force, Coulomb force is the other internal force that makes the beads interacting with each other according to the Coulomb's law. According to eq. (4), the net viscoelastic force acting on Bead i is as follows:

$$\mathbf{F}_{vi} = \frac{\pi d_{i,i+1}^2}{4}\sigma_{i,i+1}\mathbf{f}_t - \frac{\pi d_{i-1,i}^2}{4}\sigma_{i-1,i}\mathbf{f}_t \tag{22}$$

The net Coulomb force acting on Bead i from all the other beads is as follow:

$$\mathbf{F}_{ci} = \sum_{\substack{j=1, \\ j \neq i}}^{N} \frac{e^2}{R_{ij}^2} \left(\mathbf{i} \frac{x_i - x_j}{R_{ij}} + \mathbf{j} \frac{y_i - y_j}{R_{ij}} + \mathbf{k} \frac{z_i - z_j}{R_{ij}} \right) \tag{23}$$

where $R_{ij} = [(x_i - x_j)^2 + (y_i - y_j)^2 + (z_i - z_j)^2]^{1/2}$ is the distance between Bead i and Bead j.

2.2.3. Bending restoring force

When the jet segment begins to bend, it comes the surface tension to restore the segment to its rectilinear shape, which is acted as the restoring force. The restoring force acting on Bead i is given by:

$$\mathbf{F}_{bri} = \frac{\eta \pi \left(\frac{d_{i-1,\ i} + d_{i,\ i+1}}{2} \right)^2 k_i}{4(x_i^2 + y_i^2)^{1/2}} [\mathbf{i}|x_i|\text{sign}(x_i) + \mathbf{j}|y_i|\text{sign}(y_i)] \tag{24}$$

where η is the surface tension coefficient, and b_i is the curvature of jet segment and is described as $|b_i = \mathbf{R}_i' \times \mathbf{R}_i''|$.

2.2.4. Conservation law

The jet obeys the conservation of mass during the spinning process, and for each bead we get:

$$\rho_f l_{i,\ i+1} \frac{\pi d_{i,\ i+1}^2}{4} = m_0 \tag{25}$$

where m_0 is the initial mass. Since the effect of solvent evaporation on the rheological parameters of the polymer jet isn't fully known, we don't take solvent evaporation into consideration during electrospinning in this study.

In the melt blowing process, we additionally need to consider the heat transfer because the physical properties of the melt are temperature dependent. In this study, only heat transfer between the jet and air is taken into consideration and the energy equation requires:

$$m_i C_i \frac{dT_i}{dt} = -h\pi \frac{d_{i-1,\ i} + d_{i,\ i+1}}{2} \frac{l_{i-1,\ i} + l_{i,\ i+1}}{2} (T_i - T_{ai}) \tag{26}$$

where C_i is the heat capacity of polymer, T_i is the temperature of Bead i, T_{ai} is the air temperature at Bead i, and h is the air convective heat transfer coefficient.

2.2.5. Perturbation of the rectilinear segment of jet

It is known that whipping, which is triggered by lateral perturbation, is an important physical element of the spinning process for producing miro/nanofibers. During whipping, the bending path of the jet contributes to additional jet elongation and consequent jet attenuation. The initial perturbation is added by inserting small displacements to the x and y coordinates of Bead i, here M is the initial perturbation amplitude, and ω is the initial perturbation frequency.

$$x_i = M sin(\omega t) \tag{27a}$$

$$y_i = M cos(\omega t) \tag{27b}$$

2.2.6. External physical field

An airflow field and an electric field were employed throughout the melt blowing and the eletrospinning processes, respectively. The melt blowing airflow field was simulated by COMSOL Multiphysics software and the electric field simulation was carried out through Ansoft Maxwell. The simulation results of these two external physical fields are shown in Fig. 4, with the air velocity of 280 m s^{-1} and temperature of 260 °Cat the air inlet in the melt blowing process, and the applied voltage of 25 kV and spinneret-to-collector distance of 12.5 cm in electrospinning, respectively.
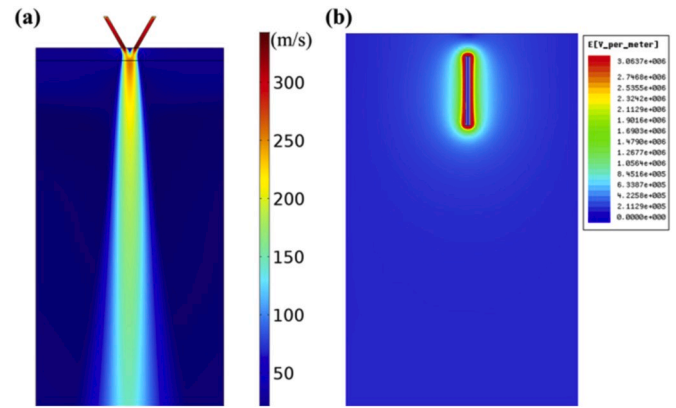

Fig. 4. (a) Velocity distribution of airflow field in the melt blowing process, **(b)** electric field distribution in electrospinning.

The formation of micro/nanofibers under external physical field is an intricate process involving mechanics and physics, where polymer jet becomes thinner and thinner due to the high-speed stretching, accompany with physical changes such as solvent evaporation, cooling and solidification. The morphology of as-prepared fibers is influenced by the difference of mechanical, rheological and physical properties within the two components in the stretching process of bi-component jet. In the spinning process, stretching not only is responsible for jet thinning but also affects the microstructure, including molecular orientation and crystallization behavior within fibers. This model only paid attention to the macroscopic morphology of the fibers without consideration of microstructure change inside fibers. Microstructure factors such as crystalline changes which may exist in certain polymers during the spinning process are not taken into consideration.

3. Experimental

3.1. Materials

Polypropylene (PP; 800 melt flow rate, MFR, at 230 °C, 0.91 g cm^{-3}, molecular mass of Mn~34000)was purchased from DAELIM, Korea, Thermoplastic Polyurethane (TPU; Elastollan 2180A10; 50 MFR at 200 °C, 1.14 g cm^{-3}, molecular mass of Mn~102000) was from BASF, Germany. Cellulose Acetate powders (CA; 39.8 wt % acetyl, molecular mass of Mn~30,000), N, N-Dimethylacetamide (DMAc; 0.937 g mL^{-1} at 25 °C), and N, N-dimethylformamide (DMF; 0.944 g mL^{-1}) were purchased from Sigma-Aldrich. Thermoplastic Polyurethane (TPU; Desmopan DP 2590A) was from Bayer Materials Science, Germany. Lithium chloride anhydrous (LiCl) was from Macklin. Acetone was from Shanghai Lingfeng Chemical Reagent Co. Ltd.. All chemicals were used as received.

3.2. Melt blowing and electrospinning

A schematic diagram of the set-ups used in the melt blowing and electrospinning processes in this study is displayed in Fig. 5. Polymer blends of PP and TPU with diverse composite ratios were melt blown to produce bicomponent fibers at the following processing conditions: air pressure of 0.3 MPa, air temperature of 260 °C, polymer feed rate of 2.6 mL min^{-1}, polymer temperature of 240 °C, and spinneret-to-collector distance of 20 cm.

Polymer solutions of TPU and CA were prepared and separately transferred into two syringes connected with the spinneret. The two polymer solutions were extruded into the spinneret to create a parallel arranged bicomponent jet with diverse feed rate ratios. The applied voltage was 25 kV. The distance from spinneret to collector was set as 12.5 cm.
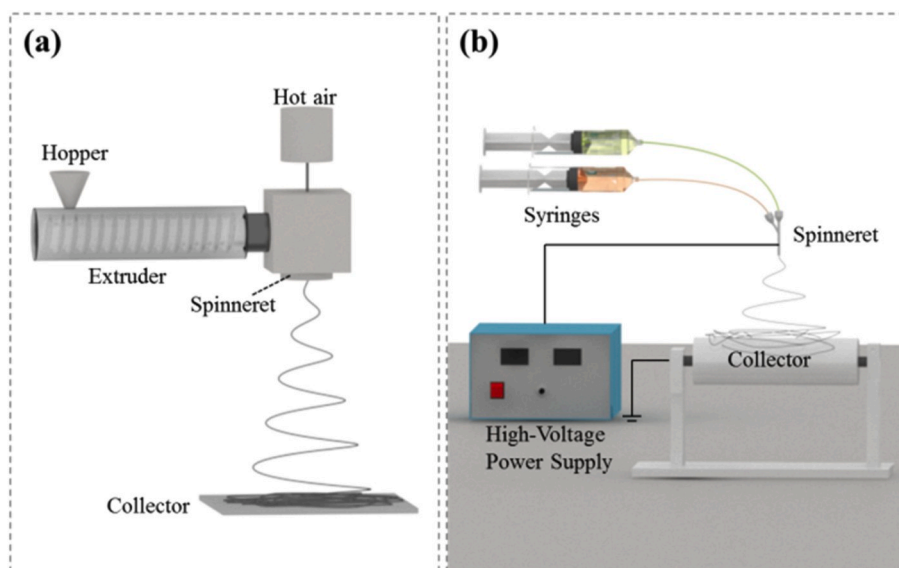
Fig. 5. Schematics of **(a)** melt blowing set-up and **(b)** electrospinning set-up.

3.3. Characterization

Samples of the as-spun composite fibers were observed under Field Emission Scanning Electron Microscope (FE-SEM, SU8010, HITACHI) after splutter with platinum under an acceleration voltage of 5 kV. Image-pro was used to measure the helical pitch and helical diameter of the obtained bicomponent helical fibers to calculate their curvatures based on 5–10 measurements of each sample.

4. Results and discussion

4.1. Strain difference and curvature

We begin with the calculation of development of strain differences, $\Delta\varepsilon_i^*$, between the two components in both the melt blowing and electrospinning processes. The polymer properties and processing parameters involved in the model are listed in Table 1. The two components involved in the melt blowing process are PP and TPU, while those used in electrospinning are CA and TPU. As we can see from Fig. 6, with the increase of the distance from the spinneret, the strains arisen in both two components grow rapidly in a short distance and then grow at a much slower rate. There is a remarkable strain difference (the red line in the figure) between the two components. The results indicate a larger strain arisen in the TPU jet under both the melt blowing airflow field and the electric field. In the region near the spinneret, where the characteristics of applied physical field and the rheological properties of the polymer components progress severely in a complex way, $\Delta\varepsilon_i^*$ increases dramatically.

The development of intrinsic curvatures of bicomponent jets produced from melt blowing and electrospinning are demonstrated in Fig. 7. We take the distance from the spinneret as the independent variable of intrinsic curvature. In the melt blowing process (Fig. 7a), the intrinsic curvature begins to increase when the bi-jet is about 8 cm away from the spinneret and the rapid increase lasts for a short distance. The

Table 1
Polymer properties and processing parameters.

Melt blowing	PP	TPU
Density ρ_f (kg m^{-3})	$1/(1.145 + 9.03 \times 10^{-4}T)$	$1/(0.891 + 4.86 \times 10^{-4}T)$
Viscosity μ (Pa s)	$6.38 \times 10^{-15}\text{Mn}^{\text{a}3.55}\exp\left\{\dfrac{-8.86(T-180)}{T-78.4}\right\}$ [20,21]	$1.1 \times 10^{-11}\text{Mn}^{3.5}\exp\left\{\dfrac{-1.86(T-280)}{T-178.4}\right\}$ [21]
Heat capacity h	$0.3669 + 2.42 \times 10^3 T$	$0.33 + 1.4 \times 10^3 T$
Elastic modulus G (Pa)	2.8×10^4	1.4×10^3
Surface tension coefficient η (kg s^{-2})	0.7	0.7

Electrospinning	CA	TPU
Density ρ_f (kg m^{-3})	1.3×10^3	1.2×10^3
Viscosity μ (Pa s)	0.741	0.621
Elastic modulus G (Pa)	2×10^{-5}	1×10^{-5}
Surface tension coefficient η (kg s^{-2})	0.035	0.037
Conductivity K (Ω m^{-1})	4.902×10^{-3}	4.902×10^{-3}

Processing condition		
Initial temperature (°C)	260	
Volume flow rate (mL min^{-1})	4.24	
Air velocity (m s^{-1})	280	
Air jet temperature at spinneret (°C)	260	
Voltage (V)	2.5×10^4	
Distance to collector (m)	0.2 (melt blowing)	
	0.125 (electrospinning)	

[a] Mn in this table is the number-average molecular weight of the polymer.
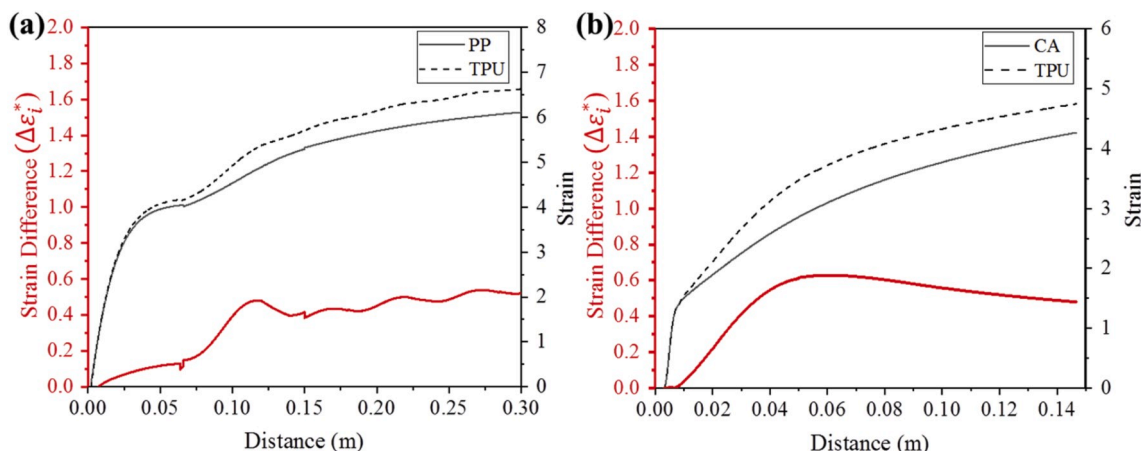
Fig. 6. Strains (black lines) of the two components of **(a)** PP and TPU in melt blowing and **(b)** TPU and CA in electrospinning and strain differences (red lines) between the two components. (For interpretation of the references to colour in this figure legend, the reader is referred to the Web version of this article.)
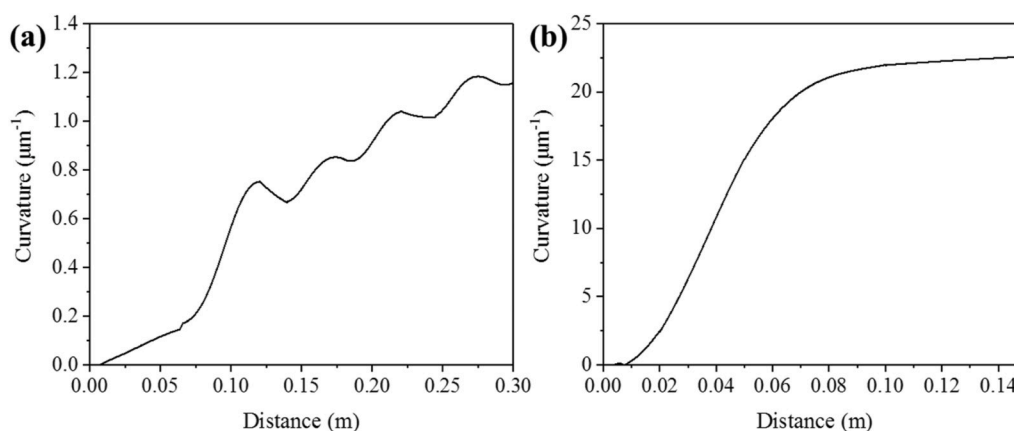

Fig. 7. The development of intrinsic curvature k_i of the bi-component jets with the growing of the distance from the spinneret **(a)** in melt blowing process with composite ratio of 3/1 (PP/TPU) and applied air velocity of 280 m s^{-1} with temperature of 260 °C and **(b)** in electrospinning process with feed rate ratio of 2/3 (CA/TPU) and applied voltage of 25 kV.

intrinsic curvature keeps increasing in a wave-like growth mode, indicating a complex process for the formation of helical structures. This may be due to the complex interplay of the aerodynamics of high-speed and high-temperature turbulent air jets with viscoelastic polymeric jet motion involved in melt blowing. As regards the intrinsic curvature in electrospinning shown in Fig. 7b, with the increase of the distance from the spinneret, the resulting intrinsic curvature first grows rapidly and then becomes gentle. It should be mentioned that the viscosity μ of the polymer components used in electrospinning keeps unchanged, unlike those used in the melt blowing process. Thus, the curve for electrospinning is relatively smooth compared to that for the melt blowing process.

4.2. Comparison of intrinsic curvature and measured curvature

The SEM images of melt-blown PP/TPU fibers and electrospun CA/TPU fibers with helical structures are displayed in Fig. 8a and b. These helical structures are considered as helixes having uniform curvatures. The curvature k is given by Ref. [15]:

$$k = \frac{r}{r^2 + \left(\frac{p}{2\pi}\right)^2} \tag{28}$$

where r is the helical radius and p is the helical pitch, which is shown in Fig. 8c. Image-pro was used to measure the helical pitch and helical
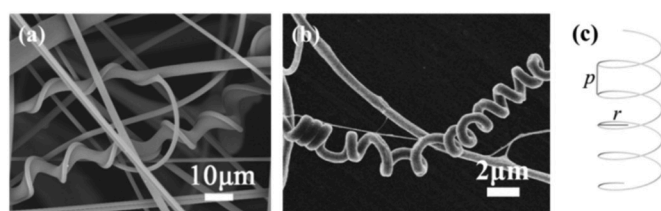

Fig. 8. SEM images of **(a)** melt-blown PP/TPU fibers and **(b)** electrospun CA/TPU fibers, **c)** a helix with radius r and pitch p.

diameter to obtain the curvatures of helical fibers based on 5–10 measurements of each sample.

The comparison of intrinsic curvature and measured curvature is carried out in electrospinning. The electrospun helical CA/TPU fibers prepared from different feed rate ratios (CA/TPU) are exhibited in Fig. 9a–e. As demonstrated in Fig. 9f, the measured curvature rises with the decrease of the feed rate ratio (i.e. the increase of feed rate of TPU) until it reaches 2/3. As depicted in Fig. 9g, with the decline of volume ratio of CA/TPU, the predicted intrinsic curvature of the CA/TPU fiber keeps growing until it reaches the maximum with corresponding volume ratio of 4/6, and then continues to drop. The values of intrinsic curvature used here were derived from k_i at the 12.5-cm distance in the curve of intrinsic curvature development. The profiles of the predicted
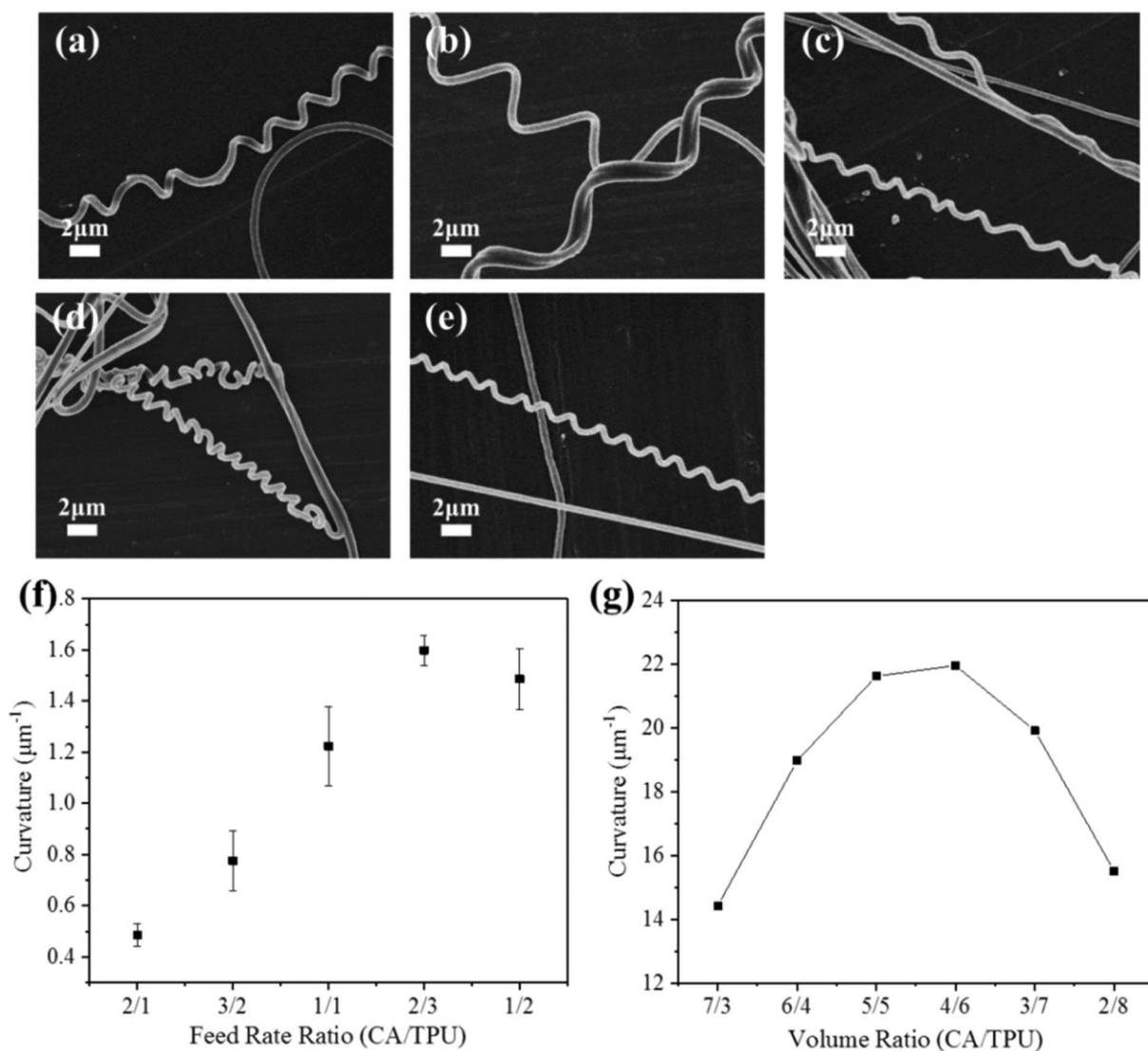
Fig. 9. FE-SEM images of electrospun CA/TPU fibers with helical structures obtained from different feed rate ratios of (a) 2/1, (b) 3/2, (c) 1/1, (d) 2/3, and (e) 1/2, (f) scatter plot of curvatures measured the from electrospun CA/TPU helical fibers prepared from different feed rate ratios, (g) line chart of calculated intrinsic curvature of electrospun CA/TPU bicomponent fibers with diverse volume ratios.

intrinsic curvature and the measured curvature agree well with each other.

Since the co-electrospinning process is relatively stable when the applied voltage is set between 20 kV and 25 kV, three different values of applied voltage was selected within the range above to discuss the effect of applied voltage on the curvature of the bicomponent fibers. The electrospun helical CA/TPU fibers prepared from different applied voltages are displayed in Fig. 10a–c. The corresponding curvatures of these prepared eletrospun fibers were measured, and the result is shown in Fig. 10d. The calculated intrinsic curvatures of electrospun CA/TPU bicomponent fibers are demonstrated in Fig. 10e. The values of intrinsic curvature used here were derived from k_i at the 12.5-cm distance in the curve of intrinsic curvature development. Both of the measured and calculated results of the curvature indicate high value of the applied voltage leads to high curvature. When the applied voltage increases to 25 kV, the curvature reaches its maximum.

In the melt blowing process, it is hard to maintain a stable spinning or to obtain normal fibers under most circumstances when the parameters were varied. Therefore, the comparison between the experimental results and the calculated results based on the theoretical model in melt blowing is not discussed in this manuscript.

4.3. Effect of parameters

The parameters involved in our model include material properties (elastic modulus, viscosity, surface tension coefficient, density, and heat capacity) and processing conditions (applied air velocity and temperature, applied voltage, volume ratio of the components), some of which are not under full control in real experiments. Based on this theoretical model, the effects of volume ratio of the components (has been studied above), elastic modulus, and intensity of the applied physical field (i.e. air velocity in melt blowing and voltage in electrospinning) on the intrinsic curvature are analyzed.

In the melt blowing process, two cases of applied air velocity, low (110 m s^{-1}) and high (280 m s^{-1}) velocities were input into the model. It is mentioned that the air velocity of 280 m s^{-1} is a commercial condition and is also used in our experiments, while 110 m s^{-1} is used as a contrast. The calculated intrinsic curvature in Fig. 11a indicates that high air velocity could lead to a high intrinsic curvature on the PP/TPU fiber. The intrinsic curvatures of the bicomponent PP/TPU fibers prepared from different volume ratios are also calculated and shown in Fig. 11b. The values of intrinsic curvature used here were derived from ki at the 20-cm distance in the curve of intrinsic curvature development.
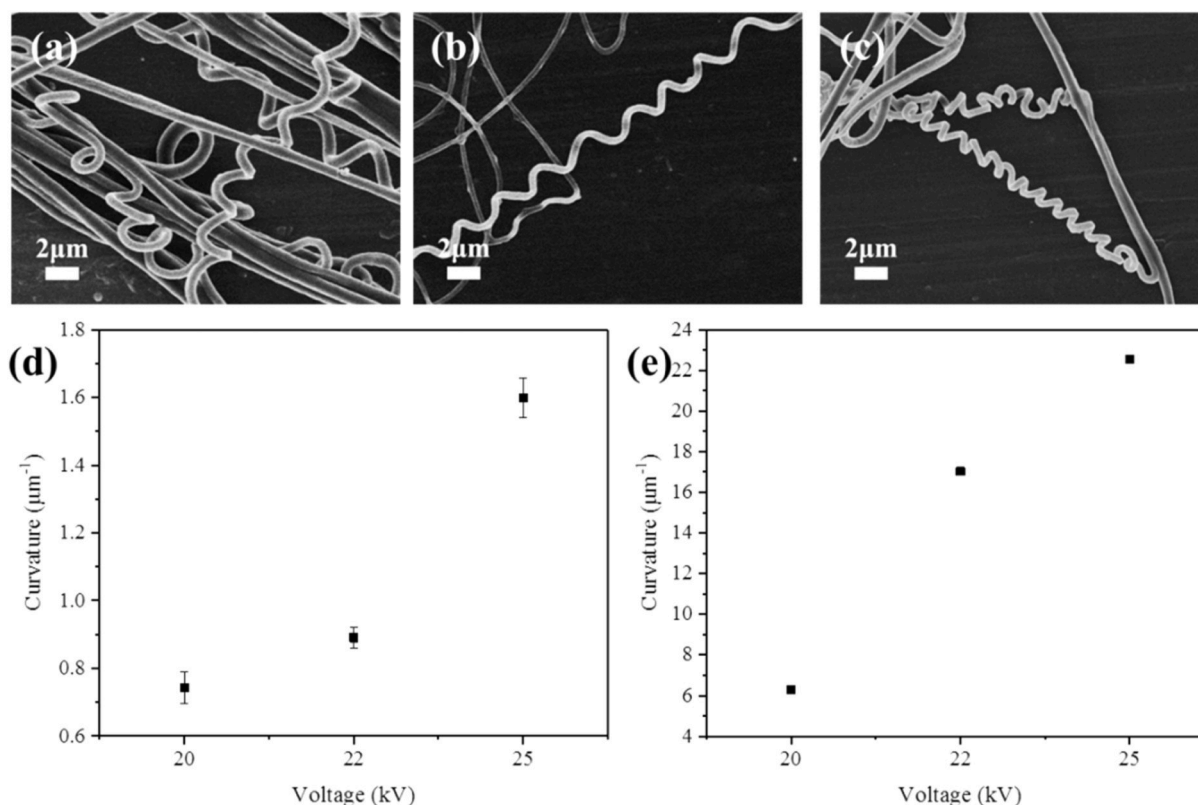
Fig. 10. FE-SEM images of electrospun CA/TPU fibers with helical structures obtained from different applied voltages of (a) 20 kV, (b) 22 kV, (c) 25 kV, (d) scatter plot of curvatures measured the from electrospun CA/TPU helical fibers prepared from different applied voltages, (e) line chart of calculated intrinsic curvature of electrospun CA/TPU bicomponent fibers with diverse applied voltages.
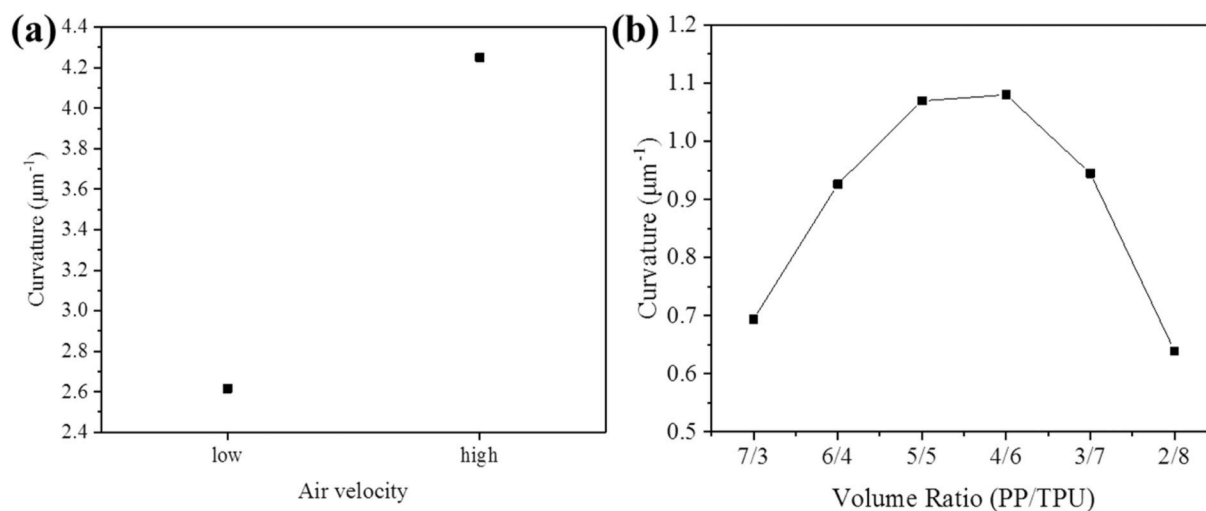

Fig. 11. Scatter plot of calculated intrinsic curvature of melt-blown PP/TPU bicomponent fibers prepared from (a) different applied air velocities and (b) different volume ratios at the 20-cm distance.

The theoretical results indicate that the intrinsic curvature of the PP/TPU fiber reaches its maximum in the case of 7/3 (PP/TPU) volume ratio and drops continuously from volume ratios of 7/3 to 9/1 (PP/TPU).

The discrepancy of elastic modulus of the involved components is closely related to the generation of strain difference in the applied physical field during spinning processes. Three elastic modulus ratios of the components 20/1, 15/1 and 10/1 in the melt blowing process and 4/

1, 2/1, 1/1 in electrospinning were input into the calculation and the results are displayed in Fig. 12, where we found the curvature increases with the increase of the elastic modulus ratio of the components.

It is predicted that exerting higher intensity of applied physical field and adopting components with greater property difference may contribute to higher intrinsic curvature of the fiber.
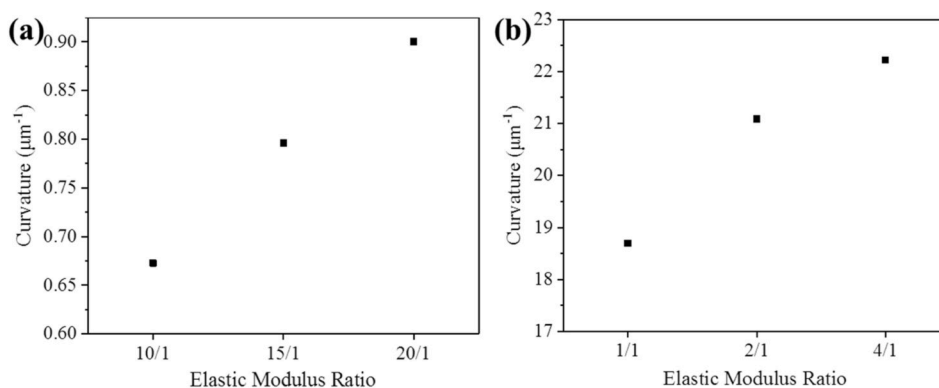
Fig. 12. Scatter plot of calculated intrinsic curvature of (a) melt-blown bicomponent fibers with different elastic modulus ratio of the components at the 20-cm distance and (b) electrospun bicomponent fibers with elastic modulus ratio of the components at the 12.5-cm distance.

5. Conclusion

A theoretical model has been developed in both melt blowing and electrospinning processes to explore the intrinsic curvature of the bicomponent fibers. The calculation result confirms that strain difference exactly exists between the two component. The curvatures of the helical melt-blown fibers and electrospun fibers were measured to make comparison with the calculation results of the intrinsic curvature of the bicomponent fibers. It turns out that the variation tendency of the predicted intrinsic curvature of the bicomponent fibers with different volume ratios is in consistent with the experimental results generally. It is predicted that exerting higher intensity of applied physical field and employing components with greater property difference may contribute to higher intrinsic curvature of the fiber. By means of this model, intrinsic curvatures can be predicted to help control the helical structure of the fibers.

Declaration of competing interest

The authors declare that they have no known competing financial interests or personal relationships that could have appeared to influence the work reported in this paper.

CRediT authorship contribution statement

Xiaomin Zhang: Conceptualization, Methodology, Software, Validation, Formal analysis, Investigation, Writing - original draft, Writing - review & editing. **Jiawei Chen:** Methodology, Software, Validation, Formal analysis, Investigation. **Yongchun Zeng:** Conceptualization, Methodology, Resources, Writing - review & editing.

Acknowledgment

References

[1] M.A.J. Uyttendaele, R.L. Shambaugh, Melt blowing - General equation development and experimental-verification, AIChE J. 36 (2) (1990) 175–186, https://doi.org/10.1002/aic.690360203.

[2] R.S. Rao, R.L. Shambaugh, Vibration and stability in the melt blowing process, Ind. Eng. Chem. Res. 32 (12) (1993) 3100–3111, https://doi.org/10.1021/ie00024a020.

[3] V.T. Marla, R.L. Shambaugh, Three-dimensional model of the melt-blowing process, Ind. Eng. Chem. Res. 42 (26) (2003) 6993–7005, https://doi.org/10.1021/ie030517u.

[4] D.H. Reneker, A.L. Yarin, H. Fong, S. Koombhongse, Bending instability of electrically charged liquid jets of polymer solutions in electrospinning, J. Appl. Phys. 87 (9) (2000) 4531–4547, https://doi.org/10.1063/1.373532.

[5] P. Dayal, T. Kyu, Dynamics and morphology development in electrospun fibers driven by concentration sweeps, Phys. Fluids 19 (10) (2007), https://doi.org/10.1063/1.2800277.

[6] I. Greenfeld, A. Arinstein, K. Fezzaa, M.H. Rafailovich, E. Zussman, Polymer dynamics in semidilute solution during electrospinning: a simple model and experimental observations, Phys. Rev. 84 (4) (2011) https://doi.org/10.1103/PhysRevE.84.041806.

[7] T. Lin, H.X. Wang, X.G. Wang, Self-crimping bicomponent nanoribers efectrospun from polyacrylonitrile and elastomeric polyurethane, Adv. Mater. 17 (22) (2005), https://doi.org/10.1002/adma.200500901, 2699.

[8] S. Chen, H. Hou, P. Hu, J.H. Wendorff, A. Greiner, S. Agarwal, Effect of different bicomponent electrospinning techniques on the formation of polymeric nanosprings, Macromol. Mater. Eng. 294 (11) (2009) 781–786, https://doi.org/10.1002/mame.200900139.

[9] S.L. Chen, H.Q. Hou, P. Hu, J.H. Wendorff, A. Greiner, S. Agarwal, Polymeric nanosprings by bicomponent electrospinning, Macromol. Mater. Eng. 294 (4) (2009) 265–271, https://doi.org/10.1002/mame.200800342.

[10] S.H. Jiang, G.G. Duan, E. Zussman, A. Greiner, S. Agarwal, Highly flexible and tough concentric triaxial polystyrene fibers, ACS Appl. Mater. Interfaces 6 (8) (2014) 5918–5923, https://doi.org/10.1021/am500837s.

[11] H.H. Wu, Y.S. Zheng, Y.C. Zeng, Fabrication of helical nanofibers via Co-electrospinning, Ind. Eng. Chem. Res. 54 (3) (2015) 987–993, https://doi.org/10.1021/ie504305s.

[12] H. Li, H. Huang, X. Meng, Y. Zeng, Fabrication of helical microfibers from melt blown polymer blends, J. Polym. Sci. B Polym. Phys. 56 (13) (2018) 970–977, https://doi.org/10.1002/polb.24618.

[13] H.H. Wu, F.G. Bian, R.H. Gong, Y.C. Zeng, Effects of electric field and polymer structure on the formation of helical nanofibers via coelectrospinning, Ind. Eng. Chem. Res. 54 (39) (2015) 9585–9590, https://doi.org/10.1021/acs.iecr.5b02882.

[14] X. Zhang, J. Chen, Y. Zeng, Construction of helical nanofibers from cellulose acetate and a flexible component, Cellulose 26 (9) (2019) 5187–5199, https://doi.org/10.1007/s10570-019-02478-x.

[15] S.J. Gerbode, J.R. Puzey, A.G. McCormick, L. Mahadevan, How the cucumber tendril coils and overwinds, Science 337 (6098) (2012) 1087–1091, https://doi.org/10.1126/science.1223304.

[16] S. Timoshenko, Analysis of Bi-metal thermostats, J. Opt. Soc. Am. 11 (3) (1925) 233–255, https://doi.org/10.1364/JOSA.11.000233.

[17] Y.C. Zeng, Y.F. Sun, X.H. Wang, Numerical approach to modeling fiber motion during melt blowing, J. Appl. Polym. Sci. 119 (4) (2011) 2112–2123, https://doi.org/10.1002/app.32921.

[18] Y.F. Sun, Y.C. Zeng, X.H. Wang, Three-Dimensional model of whipping motion in the processing of microfibers, Ind. Eng. Chem. Res. 50 (2) (2011) 1099–1109, https://doi.org/10.1021/ie101744q.

[19] J.J. Feng, Stretching of a straight electrically charged viscoelastic jet, J. Non-Newtonian Fluid Mech. 116 (1) (2003) 55–70, https://doi.org/10.1016/s0377-0257(03)00173-3.

[20] T. Chen, Study on the Air Drawing in Melt Blowing Nonwoven Process (Study on the Air Drawing in Melt Blowing Nonwoven Process), PhD Dissertation, 2003.

[21] K.F. Zieminski, J.E. Spruiell, Online studies and computer-simulation of the melt spinning of nylon-66 filaments, J. Appl. Polym. Sci. 35 (8) (1988) 2223–2245, https://doi.org/10.1002/app.1988.070350822.